Experimental and numerical simulation of a contact induced rotor/stator interaction inside an aircraft engine high-pressure compressor

Alain Batailly, Q Agrapart, A Millecamps

Experimental and numerical simulation of a contact induced rotor/stator interaction inside an aircraft engine high-pressure compressor

A. Batailly[1], Q. Agrapart[2], A. Millecamps[2]

Abstract

The development of a predictive numerical strategy for the simulation of rotor/stator interactions is a concern for several aircraft engine manufacturers. As a matter of fact, modern designs of aircraft engines feature reduced operating clearances between rotating and static components which yields more frequent structural contacts. Subsequent interaction phenomena (be it rubbing events, modal interaction or whirl motions) are not yet fully understood. For that reason, experimental data obtained from set-ups dedicated to the simulation of such interactions are scrutinized and are key in: (1) increasing the knowledge of the interaction phenomena and (2) allowing for a calibration of the numerical models with realistic events. In this contribution, the focus is made on an experimental set-up in Snecma facilities. It features a full-scale high-pressure compressor stage and aims at simulating contact induced interactions between one of the blades (slightly longer than the other ones) and the surrounding abradable coating that is deposited along the casing circumference. For this experimental set-up, it is found that the witnessed interaction involves a single blade—thus it should be analyzed as a sequence of rubbing events—and more specifically its first torsional mode, which is its second free-vibration mode. The focus is made both on the presentation of the experimental set-up and on the confrontation with the numerical results. Numerical results are analyzed by means of adaptative signal processing techniques and the consistency between numerical results and experimental observations is underlined both in time and frequency domains. In particular, the numerical strategy developed for Snecma is shown to predict very accurately the nature of the interaction as wear patterns obtained experimentally and numerically are a match. This numerical/experimental confrontation is the first attempt to calibrate a sophisticated numerical strategy with experimental data acquired within the high-pressure compressor of an aircraft engine for the simulation of rotor/stator interactions. Contrary to previous studies carried out within the low-pressure compressor of an aircraft engine, this interaction is found to be non-divergent: high amplitudes of vibration are experimentally observed and numerically predicted over a very short period of time. The ability of the numerical strategy to predict torsion induced interactions opens avenues for further analyses in turbine stages and with more sophisticated models including mistuned bladed disks and multi-stage components.

Keywords

rotor/stator interaction; rubbing; nonlinear dynamics; unilateral contact dynamics; friction; abradable coating; clearance consumption

1 - Department of Mechanical Engineering, École Polytechnique de Montréal, P.O. Box 6079, Succ. Centre-Ville, Montréal, Québec, Canada H3C 3A7

2 - Safran Aircraft Engines, site de Villaroche, Moissy-Cramayel, 77550, France

Simulation numérique et expérimentale d'un cas d'interaction rotor/stator dans le compresseur haute-pression d'un moteur d'avion

A. Batailly[1], Q. Agrapart[2], A. Millecamps[2]

Résumé

Le développement d'une stratégie numérique prédictive pour la simulation d'interactions rotor/stator est un enjeu majeur pour plusieurs constructeurs de moteurs d'avion. En effet, les moteurs les plus récents possèdent des jeux de fonctionnement réduits entre les composants tournants et statiques ce qui favorise inévitablement l'apparition de contact entre ces structures. Les phénomènes d'interaction pouvant résulter de ces contacts (qu'il s'agisse de simples contacts frottants, d'interaction modale ou de mouvements de précession) ne sont pas encore bien compris. Pour cette raison, les données obtenues expérimentalement sont analysées avec minutie, notamment pour : (1) accroître la compréhension de ces phénomènes et, (2) renforcer le caractère prédictif des outils numériques existants en permettant leur calibration. Dans cet article, on s'intéresse à un banc d'essai mis en place par la société Snecma, composé d'un étage de compresseur haute-pression à échelle une dont une des aubes, légèrement en sur-longueur, entre en contact avec le revêtement abradable déposé sur le carter. Il est observé que le phénomène d'interaction n'implique qu'une seule aube—et doit ainsi être analysé comme un évènement de contact frottant aube/carter—et plus particulièrement son premier mode de torsion, soit son second mode de vibration propre. L'article porte sur la présentation du banc ainsi que sur une confrontation avec des simulations numériques. Les résultats numériques sont analysés par le biais de méthodes adaptatives de traitement du signal. La cohèrence entre les observations expérimentales et les résultats numériques est mise en évidence dans les domaines temporel et fréquentiel. En particulier, la stratégie numérique développée pour Snecma prédit de façon très précise la nature de l'interaction puisque les motifs d'usure prédits dans le matériau abradable correspondent aux observations expérimentales. Cette confrontation expérimental/numérique est une première tentative de calibration de cette stratégie numérique au sein d'un compresseur haute-pression. L'interaction observée est non-divergente: de hautes amplitudes de vibration sont observées expérimentalement et numériquement uniquement sur un court laps de temps. La possibilité de prédire numériquement de telles interactions permet d'anticiper l'analyse d'interactions dans d'autres composants du moteurs telles que les turbines.

Mots-clés

interaction rotor/stator; frottement aube/carter; dynamique non-linéaire; dynamique du contact; frottement; revêtement abradable; consommation de jeu

1 - Département de génie mécanique, École Polytechnique de Montréal, P.O. Box 6079, Succ. Centre-Ville, Montréal, Québec, Canada H3C 3A7

2 - Safran Aircraft Engines, site de Villaroche, Moissy-Cramayel, 77550, France

NOMENCLATURE

$\delta\Omega$	angular speed step between two simulations
μ	friction coefficient
Ω_c	experimental critical angular speed
Ω_c^*	predicted numerical critical angular speed
$\Omega_{c,a}^*$	actual numerical critical angular speed
1B	first bending mode of the blade
1T	first torsional mode of the blade
2B	second bending mode of the blade
LE	leading edge
MC	middle of chord
TE	trailing edge

INTRODUCTION

The need for the improvement of modern aircraft engines efficiency motivates designers to consider reduced clearances between rotating and stationary components. As a result, structural contacts may occur in non-accidental configuration. Subsequent vibratory phenomena may involve a single blade—it is then usually referred to as *rubbing* [1, 2, 3]—, a full bladed disk and the surrounding casing—with possible *modal coincidence* yielding very high amplitudes of vibration [4, 5]—or precessional shaft motions such as *backward* or *forward whirl* motions [6, 7, 8, 9]. One usual strategy employed by engine manufacturers in order to reduce clearances involves the deposition of an abradable coating [10] along the casing contact surface. This coating acts as a sacrificial material that is worn out in the case of blade/casing contact. However, even when this coating is employed, interaction phenomena have been reported [1]. Because they may threaten the engine components' structural integrity, these interactions have been the focus of many recent studies, both numerical and experimental. In particular, the numerical simulation of rubbing events has been the centre of attention in a significant number of recent publications [11, 12, 2, 13, 14, 15, 16, 17].

In this contribution, the focus is made on an experimental test bench set-up in Snecma facilities. It features a full-scale high-pressure compressor stage and aims at simulating contact induced interactions between one of the blades (slightly longer than the other ones) and the surrounding abradable coating that is deposited along the casing circumference. For this experimental set-up, it is found that the witnessed interaction involves a single blade. Indeed, adjacent blades are also instrumented but feature negligible amplitudes of vibration. The localization of the interaction to the longer blade is also corroborated by the absence of significant amplitudes of vibration on the disk. Thus, this interaction phenomenon should be analyzed as a sequence of rubbing events and the focus is made on the identification of the blade response modal content, more specifically its first torsional mode, which is its second free-vibration mode.

The first section of the article describes the test bench and the targeted interaction scenario, it also provides details regarding the blade instrumentation as the type of gauges used during the experiment is briefly exposed. Experimental results and observations are then listed in the second section of the article. Following sections are related to the numerical investigations carried out in order to numerically predict the experimental results. The third section recalls the key points of the employed numerical strategy. Finally, in the last section, numerical results are sucritinised both in time and frequency domains and confronted with experimental observations.

Note Amplitudes are normalized with respect to reference data for confidentiality purposes.

EXPERIMENTAL SET-UP

Test bench

The experimental set-up presented in this article is part of the European research program NEWAC[1] dedicated to the reduction of CO_2 emissions and fuel consumption. More specifically, the experimental set-up is used to investigate the interaction between a full scale bladed disk of an axial high-pressure compressor and its surrounding casing. The

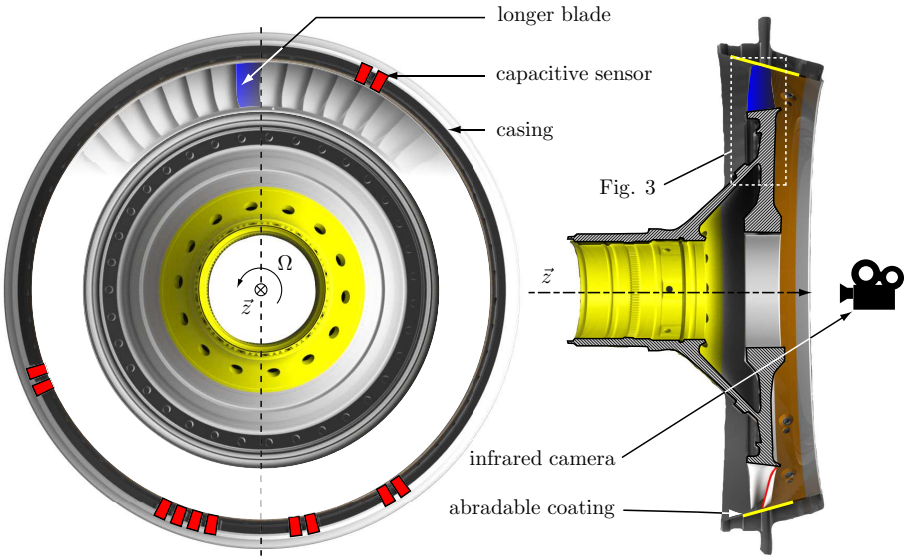

Figure 1. front view and cut view of the high-pressure compressor second stage used in the experimental set-up

bladed disk of interest is machined from a single solid piece of material, also named blisk. It is composed of titanium alloy blades and is rotationally driven by an electric motor via a flexible shaft and sealed bearings. The blisk is surrounded with a thick simplified casing on which a thick abradable coating is thermally sprayed, see Fig. 1. Adjustment screws and laminated shims allow for compensating angular misalignment and concentricity deviation between rotor and stator. The alignment is a crucial point of the experimental set-up, it has been the subject of an accurate calibration at different angular speeds to eliminate parasitic vibratory phenomena.

The rotor is cantilevered at the end of the shaft, in such a way that it allows space for an additional infrared thermal imaging camera, and easy access to the casing for clearance adjustment. The test bench is housed in a vacuum chamber in order to avoid aerodynamic effects. All tests are conducted at room temperature. Because the blisk is investigated separately from downstream and upstream stages, the applied boundary conditions are significantly different than the ones within an actual engine. Yet, these differences are assumed to be negligible which is confirmed *a posteriori* since the disk dynamics does not play a significant role in the witnessed interaction.

Blade of interest

For all blades, clearances at rest are identical from the leading edge to the trailing edge before the engine starts. Because of centrifugal effects, this clearance configuration is slightly modified at the interaction speed. Yet, numerical predictions of the blade profile at the interaction speed suggest that the clearance variation from the leading edge to the trailing edge becomes less than 2.5 % of the initial clearance at rest. With such a small difference between leading edge and trailing edge clearances, it is not expected to favor torsion modes when contact occurs. As underlined in previous work [18], clearance configuration may play a critical role in the arisal of rotor-stator interactions, but the impact of clearance configuration for our test bench goes beyond the scope of this study.

[1] http://www.newac.eu

As mentioned above, one of the blades is slightly longer than the other ones (additional length is about 1 % of the blade height) so that only this blade may impact the surrounding abradable coating deposited on the casing. The clearances are adjusted so that contacts only occur between the longer blade and the abradable coating once the targeted interaction speed Ω_c has been reached. In order to better apprehend the vibratory behaviour of the blade during the interaction, it is instrumented with two dynamic strain gauges located on its pressure side as depicted in Fig. 2. Each gauge position and orientation is carefully chosen in order to isolate the first bending mode (1B) and the first torsional mode of the blade (1T). Accordingly, these gauges will be referred to as *gauge 1B* and *gauge 1T* in the following. The acquisition frequency of these gauges, $f_a = 12,500$ Hz is chosen in order to accuratekly capture the modal participation of the blade first two free-vibration modes.

In order to ensure that the measured interaction is located on the longer blade only, the two adjacent blades and the disk are also instrumented with dynamic strain gauges. Also, it is assumed that the casing—which is particularly thick—is perfectly rigid thus casing amplitudes of vibration are not monitored.

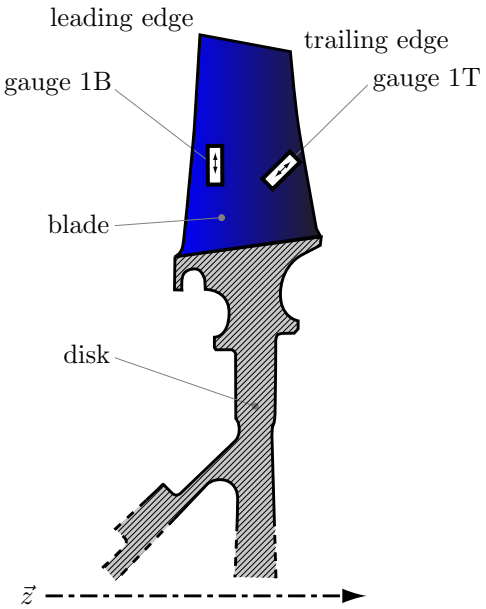

Figure 2. detailed view of the longer blade, location of gauges

Interaction scenario

The Campbell diagram pictured in Fig. 3 shows the evolution of the blade first three eigenfrequencies (the first bending mode 1B, the first torsional mode 1T and the second bending mode 2B). The dashed lines refer to the eigenfrequencies of the real blade measured experimentally at rest. The solid lines refer to the eigenfrequencies of the blade numerical model used in the following. The increase of the computed eigenfrequencies (solid lines only) over the angular speed range of interest is a consequence of centrifugal effects that are accounted for in the modal analysis. Small differences visible between the eigenfrequencies of the numerical model and the experimental blade stem from possible experimental measurements uncertainties as well as the simplification of the boundary conditions used for the numerical model. The latter is simply clamped on its root with a perfectly rigid disk, this is consistent with the aforementioned observation that the disk features negligible amplitudes of vibration.

It can be seen in Fig. 3 that the experimental angular speed Ω_c corresponds to the intersection of the 22^{nd} engine order line with the frequency line of the first torsional mode. It is also located in the vicinity of the intersection of the 8^{th} engine order line with the frequency line of the first bending mode. The same observations stand for the numerically predicted angular speed Ω_c^* for the numerical blade model. The crossing between an engine order line and an eigenfrequency line is typically an area of interest when investigating the

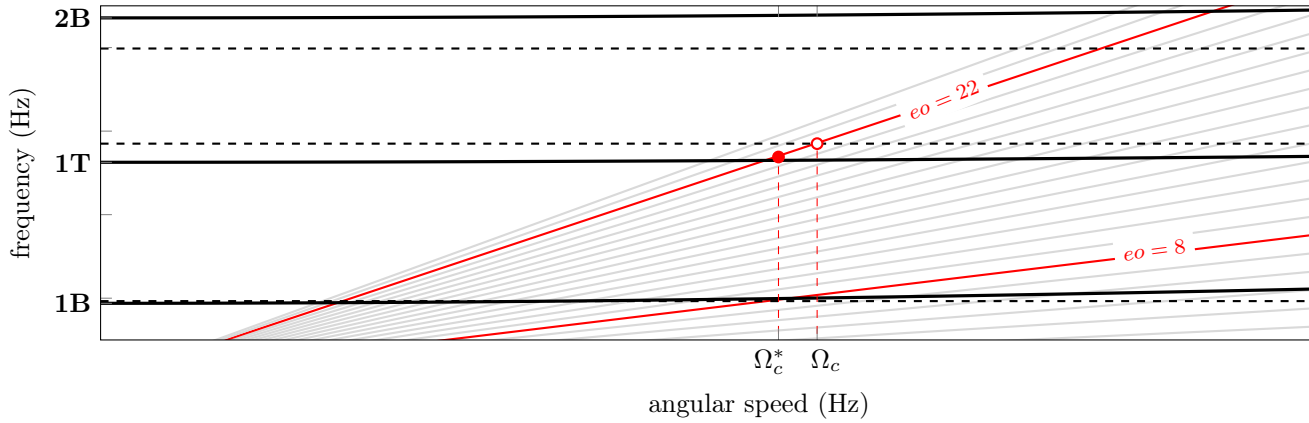

Figure 3. Campbell diagram : experimental values at rest (- - -) and numerical modal analysis (——)

vibratory response of a blade subjected to unilateral contacts conditions. As a matter of fact, this crossing implies the following relation between the eigenfrequency of the blade f_i and the angular speed Ω:

$$f_i = k\Omega, \quad k \in \mathbb{N} \tag{1}$$

meaning the blade can oscillate exactly k times over its i^{th} free-vibration mode during one revolution. The blade is thus excited over a sub-harmonic of its i^{th} eigenfrequency which may lead to a resonance in a highly nonlinear context [19, 18].

The targeted angular speed Ω_c is approached step by step as shown in Fig. 4(a). A first acceleration quickly brings the rotor to 90 % of Ω_c over the first 70 seconds of the experiment. Then, the angular speed is progressively increased and Ω_c is reached around $t = 508$ s as pictured in Fig. 4(b). The first contacts are detected around $t = 508$ s and self-sustaining interaction stops by itself at $t = 620$ s. Between these two instants, which define the time window of interest in this article, the vibratory behaviour of the blade is scrutinized in the next section.

EXPERIMENTAL RESULTS AND OBSERVATIONS

Blade vibratory response

Acquired time signals

The time signals obtained from gauges 1B and 1T (normalised strains) are respectively pictured in Fig. 5 and Fig.6. Significant amplitudes of stresses are measured for $t \in [508\,;625]$ s right after the first blade/casing contacts have occurred. Small variations of these amplitudes are noticeable for $t \in [508\,;615]$ s and a sudden very large increase of these amplitudes takes place around $t = 615$ s.

Frequency analysis for gauge 1T

The Hilbert spectrum of the time history plotted in Fig. 6 is depicted in Fig. 7. A colour code—from white for negligible amplitudes to dark blue for highest amplitudes—indicates which frequencies are dominant in the blade vibratory response over time. At the beginning of the interaction, soon after the first contacts occur, for $t \in [505\,;535]$ s, non negligible amplitudes are found in the vicinity of the first three free-vibration modes of the blade (1B, 1T and 2B). However, for $t \in [535\,;620]$ s, significant amplitudes are solely located around the first torsion mode 1T. During this period of time, the evolution of the colour of the line around mode 1T is consistent with the overall increase of amplitude seen in Fig. 6.

Abradable wear

The surface condition of the abradable coating is scrutinized after the interaction using a coordinate measuring machine. Wear levels are measured using the following resolution: 180 equidistant points in the tangential direction and 44 equidistant points in the axial direction.

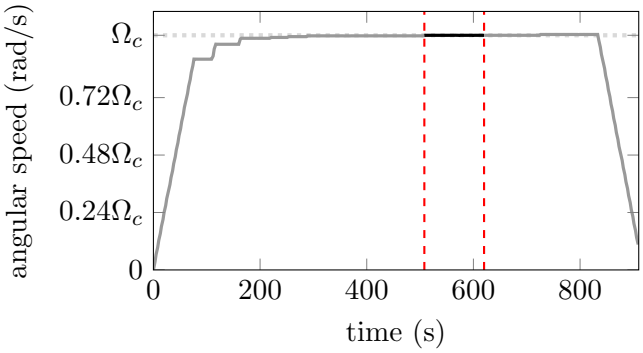

(a) whole time history

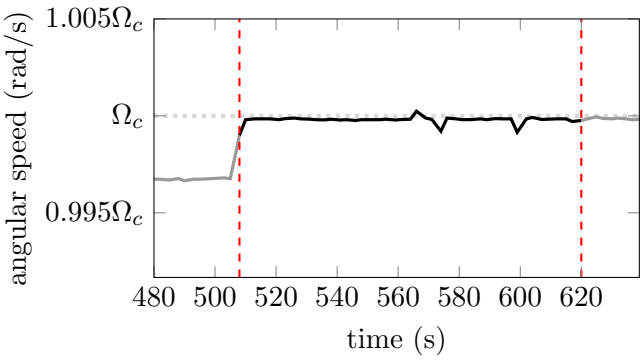

(b) zoom over the time window of interest

Figure 4. evolution of the bladed disk angular speed during the simulation

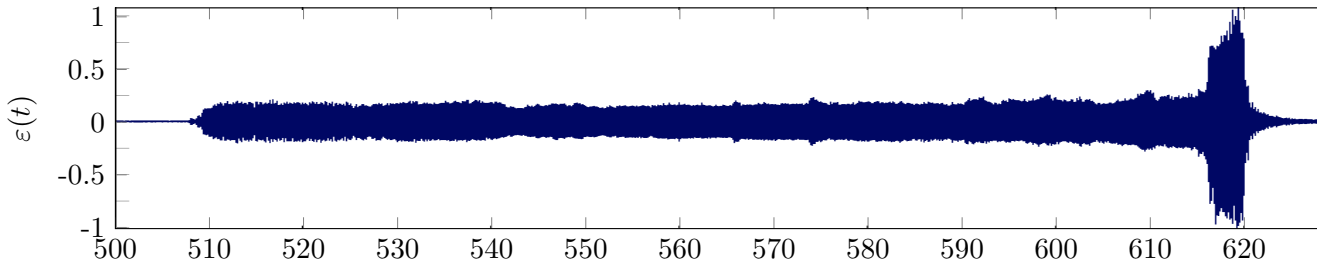

Figure 5. time signal acquired with gauge 1B

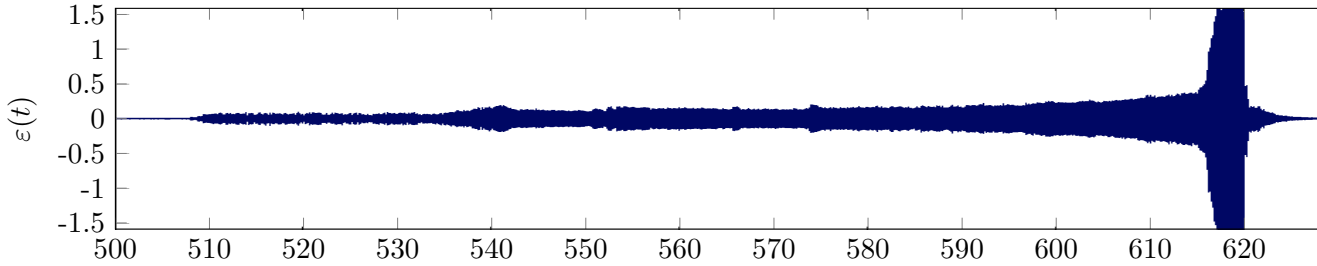

Figure 6. time signal acquired with gauge 1T

Measured data yield the wear map depicted in Fig. 8: a colour code from light blue (no wear) to dark blue (maximum wear) is used. Black areas correspond to locations that could not be measured due to the use of anchored capacitive sensors in the casing, see Fig. 1. The wear map underlines that the coating underwent severe wear during the interaction. 22 lobes are evenly located along the casing circumference in front of the blade leading edge and trailing edge. This observation is in agreement with the time domain analysis carried

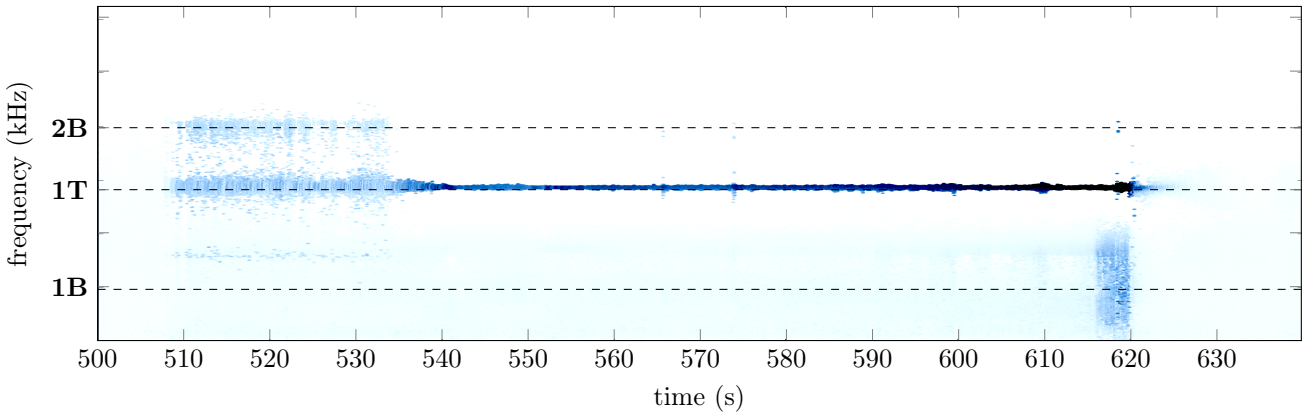

Figure 7. Hilbert spectrum of the time signal obtained from gauge 1T

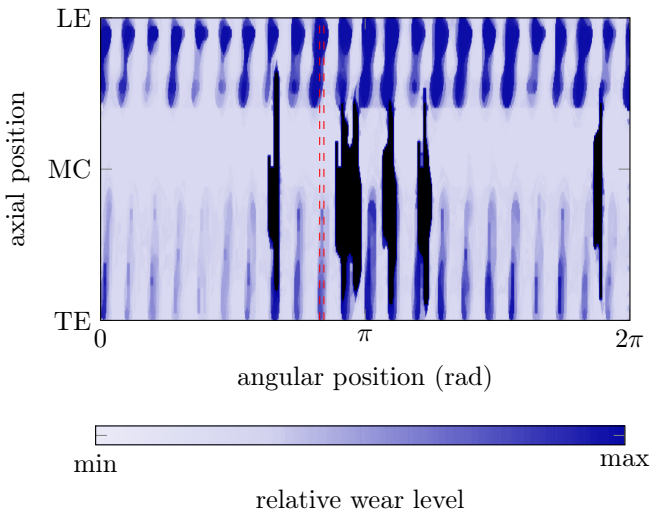

Figure 8. wear profiles measured on the casing (the vertical dashed lines (- - -) underline the angular shift between the location of leading edge and trailing edge lobes)

above. Remarkably, no significant wear level is measured in front of the middle of chord. This observation is consistent with a close inspection of the blade tip as it vibrates along its first torsion modes: indeed, it is numerically predicted (but not detailed in this article for the sake of brevity) that the blade-tip/casing clearance in front of the middle of chord does not significantly vary as the blade vibrates along this free vibration mode. When having a close look at the angular location of the wear lobes, one may notice a small yet significant angular shift between the wear lobes at the trailing edge and at the leading edge meaning that blade casing contacts did not occur at the same time on the leading edge and the trailing edge. Based on this observation and the time domain analysis carried out previously. One can only speculate that contacts must have happened two times (one contact at the leading edge followed by one contact at the trailing edge) per oscillation of the blade along its first torsional mode.

NUMERICAL MODELLING

The employed numerical strategy has been developed for Snecma [14, 19]. This strategy has been extensively detailed in previous contributions and is only briefly recalled here for the sake of brevity. It is based on an explicit time-marching algorithm [20] with a Lagrange multiplier-based contact treatment procedure ensuring that no penetration can occur between the impacting components. When contacts occur between a blade and the abradable coating, a plastic consitutive law [14] is used for modeling abradable coating removal. While this strategy allows for accounting for a full bladed disk and a flexible casing, it is here limited to a single blade and the casing is assumed perfectly rigid in agreement

with experimental observations.

Numerical framework

Same as suggested by experimental measurements, the casing is slightly ovalized. Numerically, this ovalization is used in order to initiate contacts with the blade. Numerical simulations are carried out with a constant angular speed Ω. At $t = 0$ s, the casing is perfectly circular and there is no penetration between the blade and the casing. Blade tip displacements due to centrifugal effects and casing ovalization are progressively accounted for during the first 20 % of the simulation where contact is initiated. After this point, the casing ovalization remains constant and the blade is free to interact with the abradable coating and the rigid casing.

The parameters of the simulation are as follows:

- friction is accounted for, $\mu = 0.15$, this coefficient is used for both blade/abradable coating contacts and blade/casing contacts if the abradable is locally fully removed. This value was obtained from both numerical and experimental investigations,
- the amplitude of the casing ovalization is equal to the blade/casing clearance at rest,
- the abradable coating is 5 mm thick,
- simulations are carried out over 100 blade revolutions,
- the blade modal damping coefficient is $\xi = 5 \cdot 10^{-4}$,
- empirical values are considered for the mechanical properties of the abradable coating, these values were obtained from the calibration of the employed numerical strategy with various experimental results [21, 22] :
  - Young's modulus is $E = 20$ GPa,
  - the plastic modulus is $K = 5$ GPa,
  - the yield limit is $\sigma_y = 1.5$ Pa.

The numerical convergence of the simulations has been checked with respect to the time step, the number of abradable elements as well as the blade reduction parameter but is not detailed here for brevity.

Targetted angular speed range

In order to numerically predict a rotor/stator interaction, it is first required to estimate the angular speed range over which it may occur. The Campbell diagram plotted in Fig. 3 combines the eigenfrequencies of the physical model and the numerical model. It appears that the targetted interaction is anticipated for $\Omega_c^* < \Omega_c$ since the eigenfrequency of the first torsional mode is slightly lower than the one of the physical model.

However, the stiffening effect stemming from unilateral contact constraints typically shifts the predicted interaction speed toward higher values. For that reason, numerical simulations are carried out over an angular speed range $\Omega \in [0.97\Omega_c^* \,; 1.10\Omega_c^*]$ centered on a higher value than Ω_c^*. This angular speed range also corresponds to $\Omega \in [0.9\Omega_c \,; 1.02\Omega_c]$.

In total, 101 simulations are carried out over this angular speed range, the angular speed increment between two simulations is $\delta\Omega = 0.0012\Omega_c$.

Modelling

The reduced-order model of the blade used for the simulation is computed from a 3D industrial finite element model clamped on its foot. Eight nodes are used along the blade tip in order to manage contact with the abradable coating and the casing. A Craig-Bampton based component mode synthesis method [19] is used in order to obtain a numerically efficient model. The reduced-order model contains 115 degrees of freedom, its convergence with respect to the inital finite element model with respect to the reduction parameter has been carefully checked, its first eigenfrequencies are shown in Fig. 3.

NUMERICAL RESULTS

Wear maps

At the end of each simulation, a wear profile is obtained in front of each of the eight boundary nodes along the blade tip. When put side by side, these profiles draw a wear map on which the wear level is represented by a colour code from white (no wear) to black (maximum

wear). Such wear maps are pictured in Fig. 9(a) and in Fig. 9(b) respectively for the leading edge and the trailing edge. Several wear patterns are noticeable over the angular speed range :

for $\Omega \in [0.900\Omega_c\,;0.902\Omega_c]$**:** at the very beginning of the angular speed range, significant wear levels with 9 lobes are numerically predicted. This interaction is likely to be related to the crossing of the ninth engine order line with the first bending mode frequency line, see Fig. 3 around $0.856\Omega_c$. Indeed, it has been previously observed that bending initiated interactions typically feature high amplitudes of vibration and deeper wear lobes than torsional initiated interactions [18];

for $\Omega \in [0.907\Omega_c\,;0.909\Omega_c]$**:** a narrow band of wear is noticeable, the relatively small wear levels combined with the localization of this phenomenon indicates that it may be related with a high frequency mode (bending or torsion) or potentially a sub-harmonic of a high frequency mode. The impossibility to distinguish a precise number of lobes makes it arduous to analyze further;

for $\Omega \in [0.941\Omega_c\,;0.950\Omega_c]$**:** a narrow interaction area with a high number of lobes is predicted, zoom over this area are provided for both the leading edge and the trailing edge in Fig. 9(c) and in Fig. 9(d). These figures allow for a precise count of the number of lobes: 22 wear lobes evenly spaced along the casing circumference are visible. The colour code indicates that higher wear levels are observed at the leading edge;

for $\Omega \in [0.983\Omega_c\,;0.993\Omega_c]$**:** eight lobes of relatively low depth are predicted;

for $\Omega \in [0.993\Omega_c\,;1.05\Omega_c]$**:** eight deep lobes are predicted through out this angular speed range, which coincidates with the crossing of the eighth engine order line with the first bending mode frequency line in Fig. 3. The analysis of such interaction goes beyond the scope of this article, the reader may refer to [19] for more details regarding bending induced interactions.

In the following, all the numerical results are related to $\Omega^*_{c,a} = 0.946\Omega_c$.

Wear profiles at the critical speed $\Omega^*_{c,a}$

Numerical/experimental confrontation

The wear profiles obtained from the leading edge to the trailing edge for $\Omega^*_{c,a}$ are combined in Fig. 10. The colour code used in Fig. 10 is identical to the one used in Fig. 8 and is relative: from highest wear levels pictured in dark blue to lowest wear levels in light blue. The comparison of Figs. 8 and 10 underlines that numerical results and experimental observations are consistent in terms of relative wear levels: in both cases the deepest lobes are located at the leading edge (LE) while the lobes at the trainling edge (TE) are thinner and less deep. Also, both experimental observations and numerical results suggest low to no wear facing the middle of chord. Finally, the same angular shift is found between the location of the wear lobes in front of the trailing edge and the location of the wear lobes in front of the leading edge.

All these observations confirm the fact that a linear—in the sense that the small perturbation framework is considered—finite element blade model used for the numerical simulations provides an accurate approximation of blade/casing clearances.

Frequency analysis

The radial displacement of the blade leading edge is pictured in Fig. 11. Soon after blade/abradable coating contact is initiated—around $t = 0.05$ s—significant amplitudes of vibration are predicted. These amplitudes remain steady over a few revolutions before they are amplified and reach a maximum for $t = 0.55$ s. At this precise moment, the blade did about 70 revolutions. Soon after, for $t > 0.6$ s, the amplitude of vibrations starts decreasing due to structural damping which indicates that contact has been lost.

The Hilbert spectrum of the time history depicted in Fig. 11 is shown in Fig. 12. Similarly to the Hilbert spectrum pictured in Fig. 7, significant amplitudes of vibration are represented in a time/frequency plane using the following colour code: from white (negligible amplitudes) to dark blue (highest amplitudes). Overall, two lines appear in this spectrum : (1) the first one is located slightly above the frequency of the first torsional mode 1T, it features the highest amplitudes, and (2) a second one is located slightly above the frequency of the second torsional mode 2T. This spectrum underlines that the numerically predicted

interaction is almost essentially related to torsional modes as only negligible amplitudes are visible around the frequency of the first bending mode. A close inspection of the Hilbert spectrum highlights that the location of the highest amplitudes of vibration are slightly over the frequencies of the torsional modes for $t < 0.6$ s because of contact stiffening. As a matter of fact, for $t > 0.6$ s, after contact has been lost, these amplitudes are found closer to the frequency lines as contact stiffening disappeared.

The comparison of the Hilbert spectrum in Fig. 12 with the spectrum pictured in Fig. 7 underlines that the numerically predicted interaction seems to be consistent with experimental observations. From a numerical standpoint, and in agreement with experimental data, it is predicted that the interaction starts along bending modes but related amplitudes of vibration are so small that they are hardly visible in Fig. 12 for $t \in [0\,;0.12]$ s.

However, numerical simulations fail to predict any participation of the second bending mode 2B. The participation of a mode or another in the transient phase following the first contacts is closely related to the contact configuration. It is possible that the idealized configuration used numerically is responsible for this approximation. Regarding the strong participation of the second torsional mode 2T, this numerical prediction cannot be confronted to experimental data since the eigenfrequency of this mode is higher than the acquisition frequency of gauges 1B and 1T. Because experimental and numerically predicted wear profiles are consistent, the participation of this mode in the blade dynamics on the experimental set-up cannot be ruled out.

CONCLUSION

This article describes experimental and numerical investigations carried out for the simulation of a rotor/stator interaction case within the high-pressure compressor of an aircraft engine. This interaction case is initiated by structural contacts between a blade and the surrounding casing on which is deposited an abradable coating. Because only one blade of the bladed disk is involved in the interaction, the interaction may be qualified as a rubbing event. Experimental observations underline the domination of the first torsional mode—which is the second free-vibration mode of the blade—in the blade vibratory response. It is remarkable that the simulated interaction does not diverge: it does not lead to blade failure contrary to bending induced interactions previously observed.

A reduced-order model based numerical strategy is employed for the simulation of this rubbing event. The confrontation of numerical results with experimental observations highlights the relevance of this strategy. In agreement with experimental observations, numerical results feature (1) a blade dynamics dominated by bending modes following the first contacts before torsional modes become dominant, (2) an abradable coating significantly worn out with 22 wear lobes in front of the blade trailing edge, 22 deeper lobes in front of the blade leading edge and practically no wear in front of the middle of chord, and (3) a non-divergent type of interaction motion where the blade amplitudes of vibration decrease at some point. While the number of wear lobes may have been predicted based on the considered engine order, it is yet unelucidated why this particular engine order leads to an interaction while others don't. Work is in progress in order to get a better understanding of the physical phenomena at play (including thermal effects) as well as a clarification with respect to the role of the first bending mode in the arisal of an interaction.

ACKNOWLEDGEMENT

Thanks go to Snecma for its technical and financial support.

References

[1] Millecamps, A., Brunel, J., Dufrénoy, P., Garcin, F., and Nucci, M., 2009. "Influence of thermal effects during blade-casing contact experiments". In Proceedings of the ASME 2009 IDETC & CIE Conference, ASME.

[2] Turner, K. E., Dunn, M., and Padova, C., 2012. "Airfoil deflection characteristics during rub events". *Journal of Turbomachinery,* **134**(011018-1-8).

[3] Sinha, S. K., 2005. "Non-linear dynamic response of a rotating radial timoshenko beam with periodic pulse loading at the free end". *International Journal of Non-Linear Mechanics,* **40**, pp. 113–149.

[4] Schmiechen, P., 1997. "Travelling wave speed coincidence". Ph.d. thesis, Imperial College of Science, Technology and Medecine - University of London, London, England.

[5] Batailly, A., Legrand, M., Cartraud, P., and Pierre, C., 2010. "Assessment of reduced models for the detection of modal interaction through rotor stator contacts". *Journal of Sound and Vibration,* **329**, pp. 5546–5562.

[6] Muszynska, A., 1986. "Whirl and whip-rotor/bearing stability problems". *Journal of Sound and Vibration,* **110**(3), pp. 443–462.

[7] Sinha, S., 2013. "Rotordynamic analysis of asymmetric turbofan rotor due to fan blade-loss event with contact-impact rub loads". *Journal of Sound and Vibration,* **332**(9), pp. 2253–2283.

[8] Salvat, N., Batailly, A., and Legrand, M., 2014. "Two-dimensional modeling of shaft precessional motions induced by blade/casing unilateral contact in aircraft engines". In Proceedings of the ASME Turbo Expo 2014, GT2014-25688.

[9] Parent, M.-O., Thouverez, F., and Chevillot, F., 2014. "Whole engine interaction in a bladed rotor-to-stator contact". In Proceedings of the ASME Turbo Expo 2014, GT2014-25253.

[10] Borel, M., Nicoll, A., Schlapfer, H., and Schmid, R., 1989. "The wear mechanisms occurring in abradable seals of gas turbines". *Surface & Coatings Technology,* **39**, pp. 117–126.

[11] Shen, X., Jia, J., and Zhao, M., 2007. "Numerical analysis of a rub-impact rotor-bearing system with mass unbalance". *Journal of Vibration and Control,* **13**(12), pp. 1819–1834.

[12] Arzina, D., 2011. Vibration analysis of compressor blade tip-rubbing. Master thesis, Cranfield University.

[13] Williams, R. J., 2011. "Simulation of blade casing interaction phenomena in gas turbines resulting from heavy tip rubs using an implicit time marching method". In Proceedings of the ASME Turbo Expo 2011, GT2011-45495.

[14] Legrand, M., Batailly, A., and Pierre, C., 2011. "Numerical investigation of abradable coating removal through plastic constitutive law in aircraft engine". *Journal of Computational and Nonlinear Dynamics,* **7**.

[15] Ma, H., Wang, D., Tai, X., and Wen, B., 2015. "Vibration response analysis of blade-disk dovetail structure under blade tip rubbing condition". *Journal of Vibration and Control*.

[16] Yuan, H., and Kou, H., 2014. "Compact-impact analysis of a rotating geometric nonlinear plate under thermal shock". *Journal of Engineering Mathematics,* **90**(1), pp. 119–140.

[17] Almeida, P., Gibert, C., Thouverez, F., Leblanc, X., and Ousty, J.-P., 2014. "Experimental analysis of dynamic interaction between a centrifugal compressor and its casing". In Proceedings of the ASME Turbo Expo 2014, GT2014-25223.

[18] Batailly, A., Legrand, M., Millecamps, A., and Garcin, F., 2015. "Conjectural bifurcation analysis of the contact-induced vibratory response of an aircraft engine blade". *Journal of Sound and Vibration,* **348**, pp. 239–262.

[19] Batailly, A., Legrand, M., Millecamps, A., and Garcin, F., 2012. "Numerical-experimental comparison in the simulation of rotor/stator interaction through blade-tip/abradable coating contact". *Journal of Engineering for Gas Turbines and Power,* **134**.

[20] Carpenter, N., Taylor, R., and Katona, M., 1991. "Lagrange constraints for transcient finite element surface contact". *International Journal for Numerical Methods in Engineering,* **32**, pp. 103–128.

[21] Mandard, R., Witz, J.-F., Boidin, X., Fabis, J., Desplanques, Y., and Meriaux, J., 2014. "Interacting force estimation during blade/seal rubs". *Tribology International,* **in press**.

[22] Cuny, M., Philippon, S., Chevrier, P., and Garcin, F., 2014. "Experimental measurement of dynamic forces generated during short-duration contacts: application to blade-casing interactions in aircraft engines". *Experimental Mechanics,* **54**, pp. 101–114.

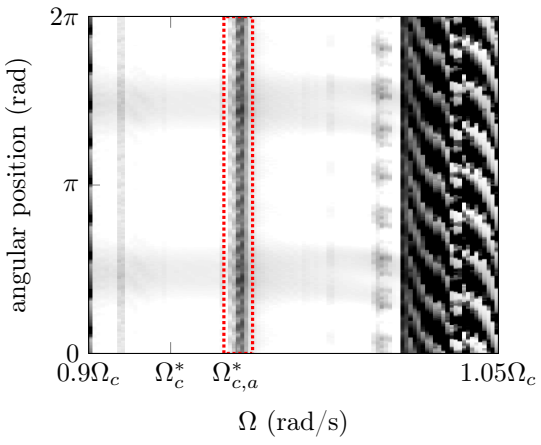

(a) leading edge

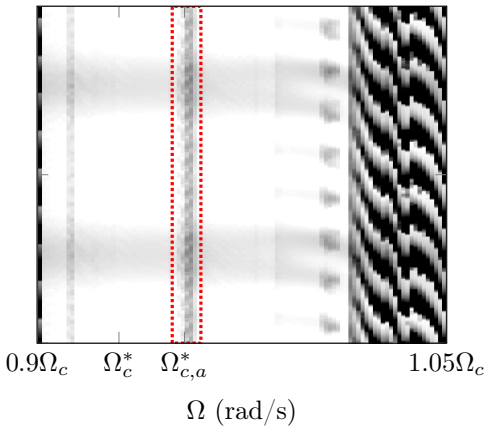

(b) trailing edge

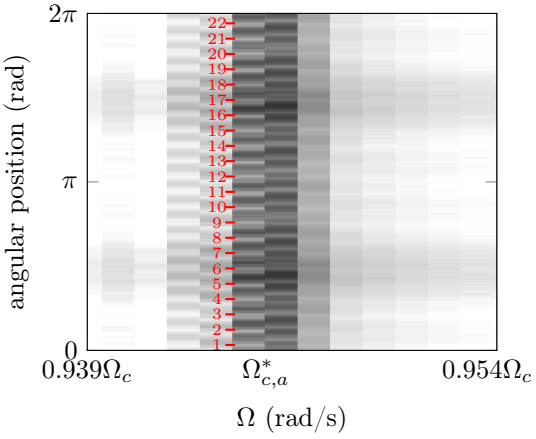

(c) leading edge (zoom)

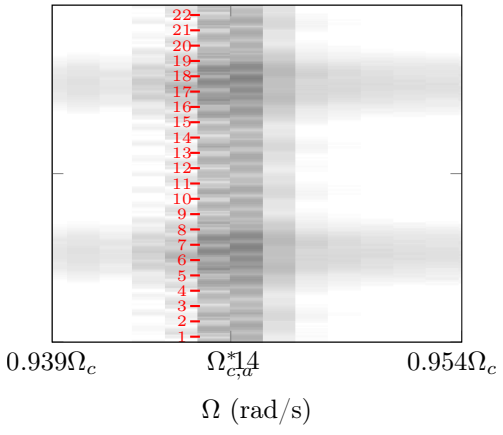

(d) trailing edge (zoom)

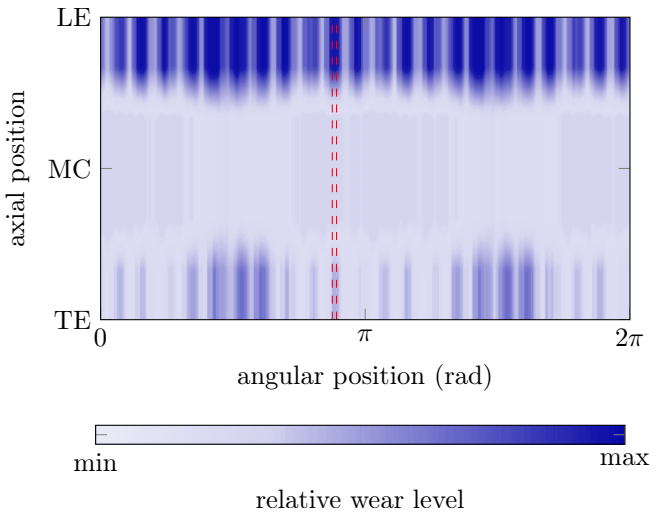

Figure 10. numerically predicted wear profiles on the casing (the vertical dashed lines (- - -) underline the angular shift between the location of leading edge and trailing edge lobes)

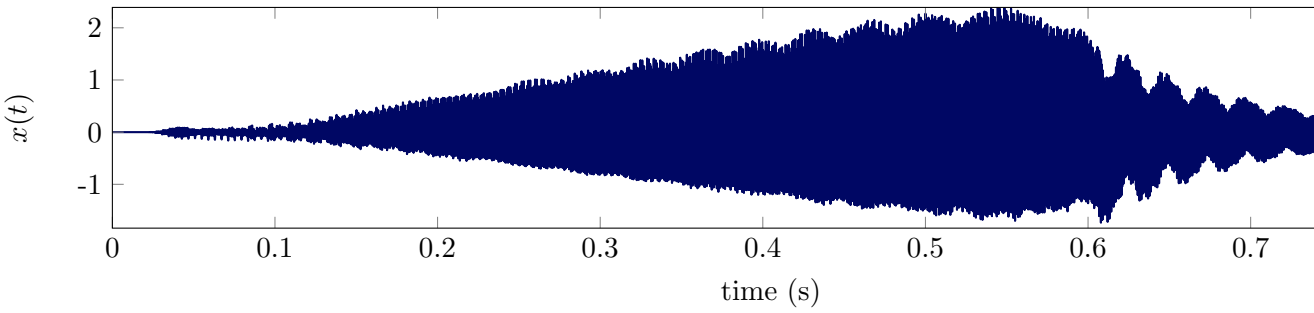

Figure 11. leading edge radial displacement

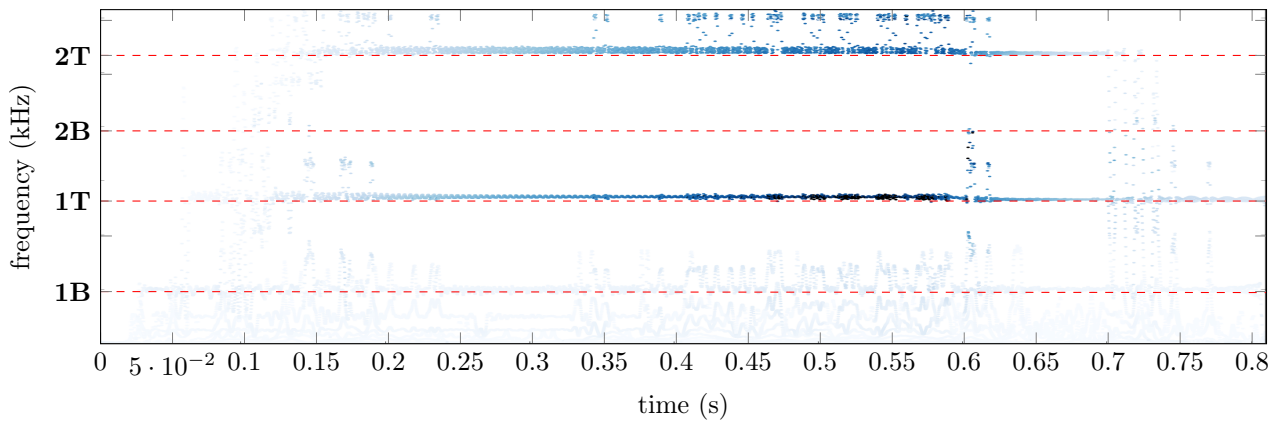

Figure 12. Hilbert spectrum of the leading edge radial displacement